Multipolar ordering from dynamical mean field theory with application to CeB₆

Multipolar ordering from dynamical mean field theory with application to CeB_6

Junya Otsuki,[1] Kazuyoshi Yoshimi,[2] Hiroshi Shinaoka,[3] and Harald O. Jeschke[1]

[1]*Research Institute for Interdisciplinary Science, Okayama University, Okayama 700-8530, Japan*
[2]*Institute for Solid State Physics, University of Tokyo, Chiba 277-8581, Japan*
[3]*Department of Physics, Saitama University, Saitama 338-8570, Japan*
(Dated: September 22, 2022)

Magnetic and multipolar ordering in f electron systems takes place at low temperatures of order 1–10 Kelvin. Combinations of first-principles with many-body calculations for such low-energy properties of correlated materials are challenging problems. We address multipolar ordering in f electron systems based on the dynamical mean-field theory (DMFT) combined with density functional theory. We derive the momentum-dependent multipolar susceptibilities and interactions by solving the Bethe-Salpeter (BS) equation of the two-particle Green's function. We apply the formalism to the prototypical example of multipolar ordering CeB_6, and demonstrate that the experimental quadrupole transition is correctly reproduced. This first-principles formalism based on DMFT and BS equation has applications which are beyond the reach of the traditional RKKY formula. In particular, more itinerant electron systems including $5f$, $4d$ and $5d$ electrons can be addressed.

I. INTRODUCTION

Recent progress in electronic structure calculations has been expanding the target of first-principles calculations to strongly correlated materials, in particular with the help of the DMFT [1–3]. The DMFT combined with density functional theory (DFT+DMFT) has been employed extensively to investigate the electronic structure of transition metal oxides [4–7], of iron based superconductors [8–10], of rare earth compounds [11, 12], and of many other materials where electronic correlations in the form of local Coulomb repulsion or Hund's rule coupling are crucial. DFT+DMFT is often employed for the theoretical support of photoemission experiments [13]. There is an ongoing effort to account for the momentum dependence of the self-energy [14], and the efficacy of new approaches is often demonstrated for the prime example of a moderately correlated oxide, $SrVO_3$. For example, DMFT has been combined with the GW method [15, 16], with vertex corrections [17, 18] or improved by the dynamical cluster approximation [19].

The descriptions of phase transitions in correlated materials is one of the objectives in DFT+DMFT investigations [20]. Typical examples include metallic ferromagnetism in elemental Fe [21–27], isostructural transitions in elemental Ce [28–32], and the orbital ordering in Cu fluorides [33, 34]. Ordered magnetism has been studied within DFT+DMFT [35–39], but such investigations are less routine than the application to paramagnetic phases. In particular, the determination of two-particle susceptibilities for comparison with inelastic neutron scattering continues to be difficult [40–43].

In this direction, multipolar ordering in rare-earth compounds is a challenging subject because of the f orbital degrees of freedom, the strong spin-orbit coupling, and the small energy scale of order $10\,\mathrm{K}$ or even less. In this paper, we address multipolar ordering based on the DFT+DMFT method. Conventionally, the multipolar ordering is considered by RKKY interactions where f electrons are treated as localized. On the other hand, a

nonmagnetic Fermi liquid (heavy fermion) ground state can be addressed from the opposite limit with itinerant f electrons. Actually, the localized and itinerant f states are continuously connected in a T-P phase diagram (Fig. 1). DMFT provides descriptions of the crossover between localized state and itinerant state including the heavy-fermion state near the quantum critical point [44–46]. Therefore, formalism based on DMFT covers the whole region of the phase diagram. This motivates us to establish descriptions of multipolar ordering based on the DFT+DMFT framework for future wider applications such as mixed-valent rare-earth compounds and actinide compounds with itinerant $5f$ electrons.

We focus on CeB_6 as a prototypical material for multipolar ordering (for a review, see Ref. [47]). The $4f^1$ configuration in trivalent Ce ions forms Γ_8 quartet ground state of the total angular momentum $j = 5/2$ under the cubic crystalline electric field (CEF) [48]. Due to the four-fold degeneracy of the CEF multiplet, CeB_6 shows a rich phase diagram as shown in Fig. 2. Two phase transitions have been observed at low temperatures [49]. Below $T_Q = 3.4\,\mathrm{K}$, CeB_6 exhibits the antiferro-quadrupole (AFQ) order of $\boldsymbol{q} = (1/2, 1/2, 1/2)$ (phase II) [50–52]. At $T_N = 2.3\,\mathrm{K}$, the antiferro-magnetic (AFM) order takes
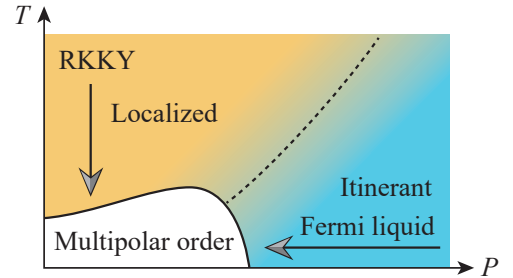

FIG. 1. A schematic P–T phase diagram of f electron materials and two contrasting approaches to the multipolar ordering.
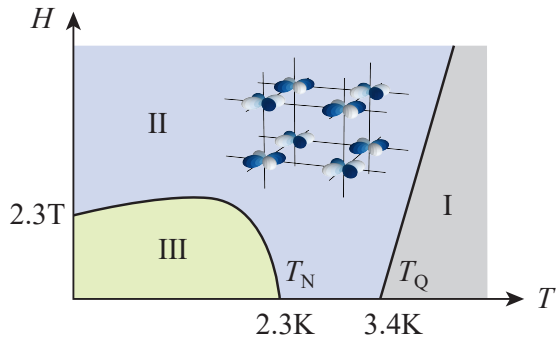
FIG. 2. A schematic T–H phase diagram of CeB$_6$ ($\boldsymbol{H} \parallel [0,0,1]$) [54, 58]. The lattice shows the configuration of the AFQ order in phase II, where the color indicates the sign of the xy-type quadrupole.

place on top of the AFQ order (phase III) [53]. Furthermore, another phase appears by partially substituting Ce with La (phase IV) [54]. This phase is ascribed to the antiferro-octupole order [55–57].

Theoretically, the phase transitions in CeB$_6$ are described by 15 multipoles in Γ_8 quartet states [59]. Since $4f$ electrons are well localized in CeB$_6$ [60], a model consisting only of the local degrees of freedom is a good starting point. Based on the Heisenberg-type model for multipoles, Shiina et al. derived the T-H phase diagram and observables related to the order parameter [61, 62]. In this approach, the coupling constants are determined so that the model yields results consistent with experiments.

Another important issue beyond phenomenology is the microscopic derivation of the multipolar interactions to understand why the multipolar ordering takes place in individual materials. Shiba et al. analyzed the RKKY formula in the Γ_8 systems and deduced general properties [63]. Evaluation of the multipolar interactions was performed later taking explicit electronic structures into account for CeB$_6$ [64–67], NpO$_2$ [68], and Pr compounds [69].

Our approach based on the DFT+DMFT method includes the RKKY formula in the strong-coupling limit [70]. In the following, we present an application of the DFT+DMFT method to CeB$_6$ and reproduce the experimental order parameter. Through this calculation, we shall establish how to fix parameters such as the Coulomb repulsion U so that the method is applicable to other materials without any tuning parameter.

II. SINGLE-PARTICLE PROPERTIES

A. DFT calculations

The starting point of our study is a precise DFT calculation for CeB$_6$. We determine its fully relativistic

electronic structure using the full potential local orbital (FPLO) basis set [71]. The calculations are performed based on a single crystal X-ray diffraction structure determined at $T = 165$ K [72]. It has a cubic space group $Pm\bar{3}m$ and features one Ce atom in the corner of the cubic cell and a B$_6$ octahedron in its center as shown in the inset of Fig. 3 (b). The DFT bands are shown in Fig. 3 (a) (full lines). We use symmetry protected maximally projected Wannier functions [73, 74] to construct a 72 band model consisting of Ce $4f$ and $5d$ as well as B $2s$ and $2p$ orbitals; the resulting tight binding representation of the bands is shown as dashed lines in Fig. 3 (a). Figure 3 (b) shows the density of states (DOS). The Ce $4f$ partial DOS is resolved by the total angular momentum j contributions. The energy splitting Δ_{SOC} between $j = 5/2$ and $j = 7/2$ due to the spin-orbit coupling (SOC) is $\Delta_{\text{SOC}} = 0.32$–$0.34$ eV, which is comparable to the value in Ce ion. The CEF splitting between the Γ_8 quartet ground state and the excited Γ_7 doublet is 11.3 meV (≈ 131 K), which is smaller by a factor of 4 compared to the experimental value 540 K [48].

B. DMFT calculations

Within the DFT+DMFT method, the single-particle Green's function matrix $\hat{G}(\boldsymbol{k}, i\omega_n)$ is given by [2]

$$\hat{G}(\boldsymbol{k}, i\omega_n) = [(i\omega_n + \mu)\hat{I} - \hat{H}_{\text{DFT}}(\boldsymbol{k}) - \hat{\Sigma}_{\text{loc}}(i\omega_n) + \hat{\Sigma}_{\text{DC}}]^{-1}, \tag{1}$$

where quantities with hat stand for 72×72 matrices. ω_n is the Matsubara frequency, μ is the chemical potential, and $\hat{I}$ is the identity matrix. $\hat{H}_{\text{DFT}}(\boldsymbol{k})$ denotes the non-interacting tight-binding Hamiltonian constructed by the DFT calculations. $\hat{\Sigma}_{\text{loc}}(i\omega_n)$ is the local self-energy in DMFT, and $\hat{\Sigma}_{\text{DC}}$ is the double-counting (DC) correction.

The local self-energy $\hat{\Sigma}_{\text{loc}}(i\omega_n)$ is computed by solving the effective impurity problem for f orbitals. We treat only $j = 5/2$ states, neglecting $j = 7/2$ states (j-j coupling scheme). The influence of the neglected $j = 7/2$ multiplet was analyzed in detail in Refs. 75 and 76. We employ fully rotationally invariant Slater interactions, which are specified by four parameters called Slater integrals F_0, F_2, F_4, and F_6. We use the standard parameterization that relates the Slater integrals to two intuitive parameters, the Coulomb repulsion U and the Hund's coupling J_{H} [77].

We represent the DC self-energy in a simple form

$$\hat{\Sigma}_{\text{DC}} = -\Delta\epsilon_f \hat{N}_f, \tag{2}$$

where $\hat{N}_f$ is a projection onto f orbitals. $\Delta\epsilon_f$ stands for the energy shift of the single-particle energy of the f electrons. This expression is motivated by the fact that the local electronic structure such as the SOC and the CEF are already taken into account by the DFT and do not need to be changed. The $\hat{\Sigma}_{\text{DC}}$ cancels only the
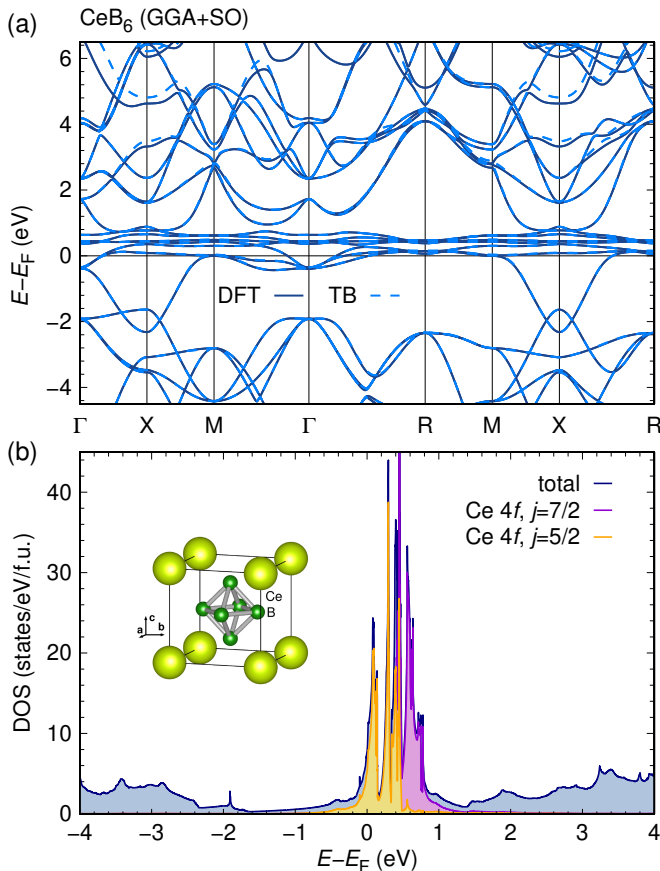
FIG. 3. (a) Fully relativistic band structure of CeB_6 (full lines), shown together with the tight binding bands obtained from projective Wannier funcions (dashed lines). High symmetry points of the cubic $Pm\bar{3}m$ space group are $\Gamma = (0,0,0)$, R = $(1/2, 1/2, 1/2)$, M = $(1/2, 1/2, 0)$, X = $(1/2, 0, 0)$. (b) Total and orbital-resolved density of states. The $Pm\bar{3}m$ crystal structure of CeB_6 is shown as inset.

averaged Hartree shift in $\hat{\Sigma}_{loc}(i\omega_n)$ so that $4f$ electrons remain on the Ce atom.

We thus have 3 parameters to determine: U, J_H, and $\Delta\epsilon_f$. We determine these parameters so that the calculated single-particle excitation spectrum agrees with the experimental and theoretical PES and BIS spectra. Two energies characterize the spectrum: Δ_- is the minimum excitation energy from the occupied $4f^n$ multiplet to the Fermi energy E_F, and Δ_+ is the minimum excitation energy from E_F to empty $4f^{n+1}$ multiplets. Table I summarizes Δ_- and Δ_+ in the literature. From the PES experiment in CeB_6, Δ_- has been reported to be $\Delta_- = 1.9$ eV. On the other hand, the BIS spectrum is not available for CeB_6. We instead refer the the data for elemental Ce. The experiment reported $\Delta_+ = 3.46$ eV, while theoretical calculation yields $\Delta_+ = 3.1$ eV. We adopt the theoretical value, since the theoretical result for Δ_- in Ce agrees with the PES value for CeB_6. From these observations, we adopt $\Delta_- = 1.9$ eV and $\Delta_+ = 3.1$ eV.

The DFT+DMFT cauculations were performed using open source software `DCore` [83] implemented on

TABLE I. Summary of the energy separation between occupied $4f^1$ state and Fermi level Δ_- and between occupied $4f^1$ state and lowest lying $4f^2$ state Δ_+ in units of eV.

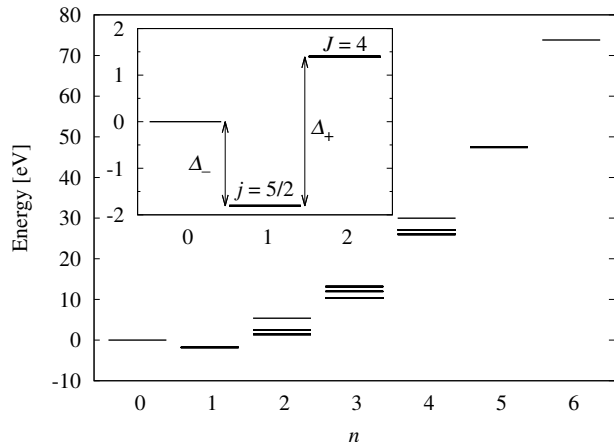| material	Δ_-	Δ_+
CeB_6 (experiment)	1.9 [78, 79]	−
Ce (experiment)	0.27–1.92 [80]	3.46 [80]
Ce (theory)	1.9 [81]	3.1 [82]

FIG. 4. Eigenenergies of the many-body states of local $4f$ electrons. The inset shows a zoom up of the low-energy multiplets.

`TRIQS` [84] and `DFTTools` [85] libraries. We solved the effective impurity model by exact diagonalization. The exact diagonalization was performed with `pomerol` [86]. Here, we neglected the effective hybridization $\Delta(i\omega_n)$. This corresponds to the Hubbard-I approximation, which is often used for descriptions of properties of rare-earth compounds [87–90]. In CeB_6, the Fermi surface is quite similar to that of LaB_6 [60], indicating that the $4f$ electrons are well localized. Therefore, a reasonable description by the Hubbard-I approximation is expected.

Without $\Delta(i\omega_n)$, energy levels of the many-body $4f$ states are well defined. Figure 4 shows the eigenvalues of the $4f^n$ multiplets for $U = 6.2$ eV, $J_H = 0.8$ eV, and $\Delta\epsilon_f = -1.6$ eV. Our way to determine these values is discussed in detail in Appendix A. The corresponding Slater integrals are $F_0 = 6.2$ eV, $F_2 = 9.54$ eV, $F_4 = 6.37$ eV, and $F_6 = 4.71$ eV. There are $2^6 = 64$ levels in this figure. The CEF splitting is not visible on this scale, and we discuss only the multiplets labeled by the total angular momentum J. The energy of the $j = 5/2$ multiplet of the $4f^1$ configuration is $E_1 = -1.9$ eV ($\Delta_- = -E_1$). The $4f^2$ configuration has three multiplets, $J = 4, 2, 0$. The Hund's ground state $J = 4$ is located at $E_2 = +1.2$ eV, thus $\Delta_+ = E_2 - E_1 = 3.1$ eV.

The final results for the single-particle excitation spectrum $A(\boldsymbol{k}, \omega)$ and the $\boldsymbol{k}$-integrated spectrum $A(\omega)$ are shown in Fig. 5. The $4f$ peaks near E_F in the DFT result [Fig. 3 (b)] are moved away from E_F in the presence of interactions. The peak at -1.9 eV corresponds to
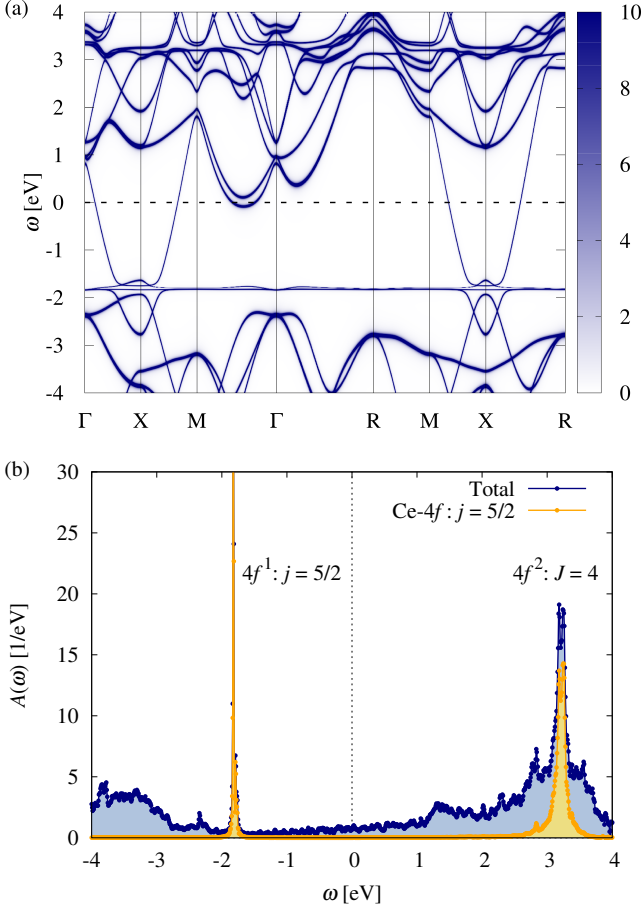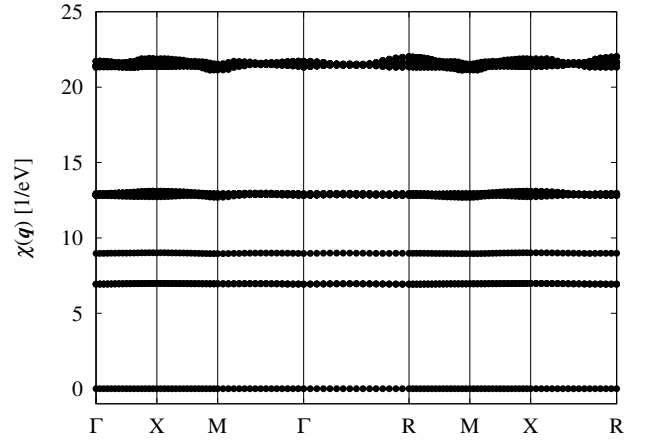
FIG. 6. The q-dependence of 36 eigenvalues of the susceptibility matrix $\hat{\chi}(q)$ in $j = 5/2$ states. $T = 0.01\,\text{eV}$.

FIG. 5. (a) The single-particle excitation spectrum $A(\boldsymbol{k}, \omega)$ computed within DMFT. Only $j = 5/2$ states are retained. (b) The $\boldsymbol{k}$-integrated spectrum $A(\omega)$ at a temperature $T = 0.01\,\text{eV}$.

$j = 5/2$ multiplet of the $4f^1$ configuration, and the peak at 3.1 eV corresponds to the $J = 4$ multiplet of the $4f^2$ configuration. The resultant energy dispersion near E_F is similar to LaB_6 [60, 91]. A parabolic band around the X point forms a Fermi surface that are connected on the Γ–M line. The occupied part of our spectral function, Fig. 5 (a), agrees very well with photoemission experiment [92] and is therefore a good starting point for the determination of two-particle quantities.

III. TWO-PARTICLE PROPERTIES

A. Multipolar susceptibility

The static susceptibility describing fluctuations within $j = 5/2$ states is given by

$$\chi_{m_1 m_2, m_3 m_4}(\boldsymbol{q}) = \int_0^\beta d\tau \langle O_{m_1 m_2}(\boldsymbol{q}, \tau) O_{m_4 m_3}(-\boldsymbol{q}) \rangle. \tag{3}$$

Here, the argument τ stands for the Heisenberg operator. The operator $O_{mm'}(\boldsymbol{q})$ is the Fourier transform of the local density operator defined by

$$O_{mm'}(i) = f_{im}^\dagger f_{im'}, \tag{4}$$

where $f_{im}^\dagger$ and f_{im} are the creation and annihilation operator for f electrons, respectively. The subscript m stands for the eigenvalues of j_z, namely, $m = -5/2, -3/2, \cdots, +5/2$. Therefore, there are $6^2 = 36$ components in the density operators, and $36^2 = 1{,}296$ components in the susceptibility. Regarding $O_{mm'}$ as a vector, $\chi_{m_1 m_2, m_3 m_4}$ can be regarded as a (36×36) matrix, which we denote by $\hat{\chi}(\boldsymbol{q})$.

In DMFT, $\hat{\chi}(\boldsymbol{q})$ can be computed by solving the BS equation of the two-particle Green's function [1, 93]. The two-particle Green's function depends on two fermionic Matsubara frequencies in addition to four m indices. We introduced a cutoff $\omega_{\max}$ for the frequency and solved the matrix equation of size $(36N_\omega \times 36N_\omega)$, where N_ω is the number of Matsubara frequencies below $\omega_{\max}$. All figures presented hereafter are results computed with $N_\omega = 160$ at $T = 0.01\,\text{eV}$ ($\omega_{\max} \approx 5.1\,\text{eV}$), unless otherwise specified. For quantitative discussions, we extrapolate results to $\omega_{\max} \to \infty$ using results computed with up to $N_\omega = 400$.

Figure 6 shows the eigenvalues of the susceptibility matrix. There are 36 eigenvalues, which are classified into 5 groups. The leading group contains $15 = 4^2 - 1$ eigenvalues, which correspond to multipolar fluctuations within Γ_8 quartet states. The second group contains 16 eigenvalues, which arise due to mixing between Γ_8 and Γ_7 states (two times 4×2). The third largest is the single fluctuation mode with A_{1g} symmetry (hexadecapole). The fourth largest (second smallest) eigenvalues group contains $3 = 2^2 - 1$ fluctuation modes, which correspond to the spin fluctuations within Γ_7 doublet states. The lowest (almost zero) single-mode fluctuation is the charge fluctuation.

TABLE II. The basis functions of 15 multipoles in the Γ_8 quartet system classified by the rank and irreducible representations (irreps). Extracted from Ref. [47].

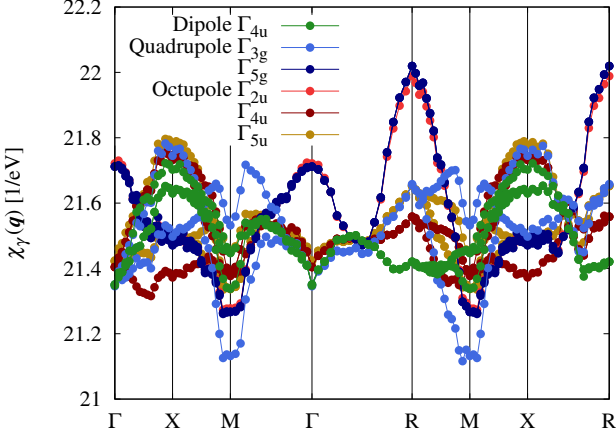|	Irrep	Basis
Dipole	Γ_{4u}	$\{x,\ y,\ z\}$
Quadrupole	Γ_{3g}	$\{3z^2 - r^2,\ \sqrt{3}(x^2 - y^2)\}$
	Γ_{5g}	$\{xy,\ yz,\ zx\}$
Octupole	Γ_{2u}	xyz
	Γ_{4u}	$\{x(5x^2 - 3r^2),\ y(5y^2 - 3r^2),\ z(5z^2 - 3r^2)\}$
	Γ_{5u}	$\{x(y^2 - z^2),\ y(z^2 - x^2),\ z(x^2 - y^2)\}$

FIG. 7. The $\boldsymbol{q}$ dependence of 15 multipolar susceptibilities $\chi_\gamma(\boldsymbol{q})$ within Γ_8 states.

The eigenvectors of the susceptibility matrix yield multipoles that take the crystal symmetry into account. Instead, we can take linear combinations of $O_{mm'}$ using pre-computed coefficients $C^{(\gamma)}_{mm'}$, namely,

$$O_\gamma = C^{(\gamma)}_{mm'} O_{mm'}, \qquad (5)$$

where the subscript γ distinguishes the irreducible representations. In point group O_h, 15 operators in the Γ_8 quartet system (excluding the charge) are classified into 6 kinds of multipoles according to the rank and irreducible representations [47, 62, 94]. Table II summarizes the basis function of these multipoles. The corresponding expressions for $C^{(\gamma)}_{mm'}$ can be constructed from the basis set [47, 62, 94]. We adopted a normalization $\sum_{mm'} |C^{(\gamma)}_{mm'}|^2 = 1$. The multipolar susceptibilities $\chi_\gamma(\boldsymbol{q})$ can then be evaluated by taking linear combinations of $\chi_{m_1 m_2, m_3 m_4}(\boldsymbol{q})$ according to

$$\chi_\gamma(\boldsymbol{q}) = \sum_{m_1 m_2 m_3 m_4} C^{(\gamma)}_{m_1 m_2} \chi_{m_1 m_2, m_3 m_4}(\boldsymbol{q}) C^{(\gamma)*}_{m_3 m_4}. \qquad (6)$$

Figure 7 shows 15 susceptibilities $\chi_\gamma(\boldsymbol{q})$ within the Γ_8 states. The leading fluctuations are the quadrupoles of Γ_{5g} symmetry at the R point $[\boldsymbol{q} = (1/2, 1/2, 1/2) \equiv \boldsymbol{q}_R]$. This is consistent with the AFQ order of phase II in CeB$_6$. The second largest fluctuation is the octupole fluctuation

of Γ_{2u} type, which is almost degenerate with the leading quadrupolar fluctuation. We will discuss this degeneracy later in the context of the multipolar interactions.

In order to determine the transition temperature, we need to decrease T to detect a divergence of $\chi_\gamma(\boldsymbol{q})$ (see for example Ref. [23]). However, it is practically difficult to perform the computations down to the expected transition temperature of order 1–10 K because the required number of Matsubara frequency, N_ω, grows in inversely proportional to T. Hence, we adopt another strategy, namely, of extracting the effective intersite interactions.

B. Multipolar interactions

If the $4f$ electrons are well localized, we expect that a description using an effective Heisenberg-type model with multipolar degrees of freedom is a reasonable approximation. In this case, $\hat{\chi}(\boldsymbol{q})$ computed by solving the BS equation follows the form $\hat{\chi}(\boldsymbol{q}) \approx [\hat{\chi}^{-1}_{\text{loc}} - \hat{I}(\boldsymbol{q})]^{-1}$, since DMFT treats intersite correlations at a mean-field level. Assuming this expression, we *define* the effective intersite interaction $\hat{I}(\boldsymbol{q})$ by

$$\hat{I}(\boldsymbol{q}) \equiv \hat{\chi}^{-1}_{\text{loc}} - \hat{\chi}(\boldsymbol{q})^{-1}. \qquad (7)$$

Once $\hat{I}(\boldsymbol{q})$ is obtained, we can extrapolate $\hat{\chi}(\boldsymbol{q})$ to lower temperatures because the dominant temperature dependence arises from $\hat{\chi}_{\text{loc}} \propto 1/T$ in localized $4f$ electron systems. We note that in the actual evaluation of $\hat{I}(\boldsymbol{q})$, the charge fluctuation has to be eliminated to avoid numerical instability in the matrix inversion (see Appendix B).

Figure 8 shows $I_\gamma(\boldsymbol{q})$ plotted separately for each irreducible representation. Here, positive (negative) values enhance (suppress) the fluctuations. The largest interaction is the quadrupole of Γ_{5g} type at the R point, which induces the AFQ order in phase II. We express this interaction by $I_Q(\boldsymbol{q}_R)$. Figure 8 indicates that the interaction strength of $I_Q(\boldsymbol{q}_R)$ is about 1 meV. An extrapolation to $\omega_{\text{max}} \to \infty$ yields $I_Q(\boldsymbol{q}_R) \approx 1.9$ meV (see Appendix C for details). The transition temperature can be determined by the condition

$$\chi_{\text{loc}} I_Q(\boldsymbol{q}_R) = 1. \qquad (8)$$

Within the Hubbard-I approximation, the local susceptibility χ_{loc} follows the Curie law $\chi_{\text{loc}} = 1/4T$, where we used $\sum_{mm'} |C^{(\gamma)}_{mm'}|^2 = 1$ and the factor 4 is due to the dimension of the Γ_8 states. Then, the transition temperature T_Q is estimated to be $T_Q = I_Q(\boldsymbol{q}_R)/4 \approx 0.48$ meV ≈ 5.6 K. This is consistent with the experimental value $T_Q = 3.4$ K.

The second largest interaction is the octupole of Γ_{2u} type. This result is consistent with the general conclusion in Ref. 63: "If the AFQ interaction of Γ_{5g} type is strong, the antiferro-octupolar interaction of Γ_{2u} type is equally strong". The Γ_{2u}-type antiferro-octupolar interaction plays a relevant role in stabilizing the AFQ ordering in phase II under magnetic field [47, 62].

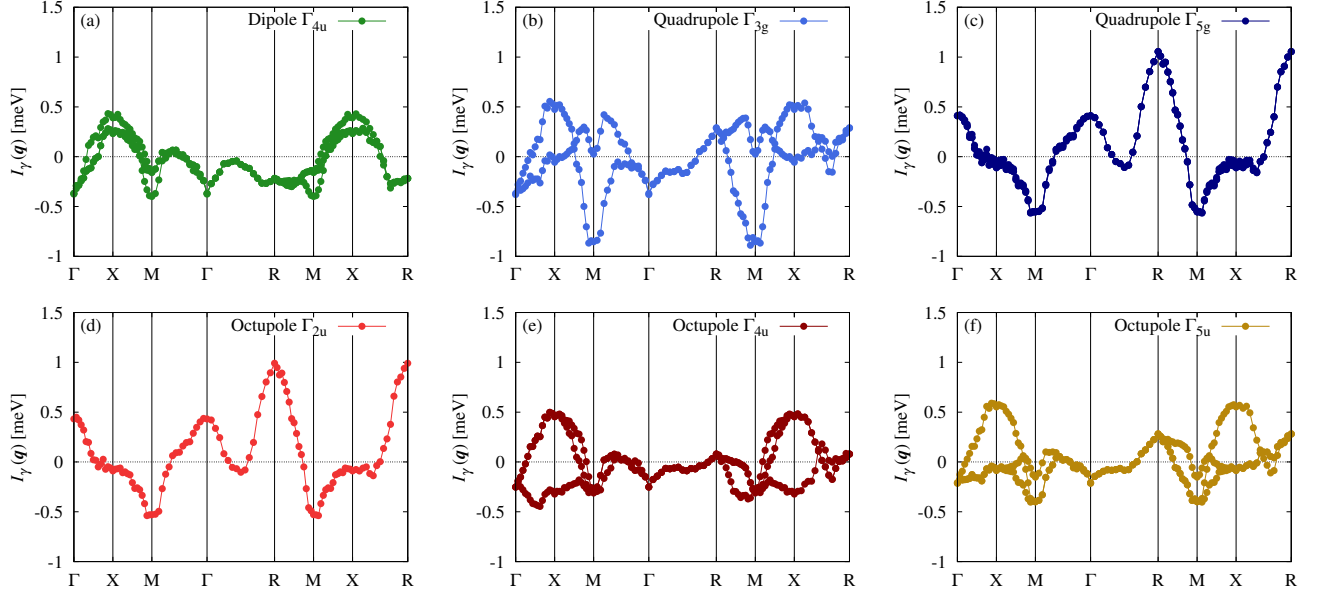FIG. 8. The $\boldsymbol{q}$ dependence of the multipolar interactions $I_\gamma(\boldsymbol{q})$ within Γ_8 states. Six kinds of multipoles are plotted separately. From (a) to (f) correspond to top to bottom in Table II.

The order parameter in phase IV is reported as the octupole of Γ_{5u} type with $\boldsymbol{q} = \boldsymbol{q}_R$ [47]. Our result shows that the octupolar interaction of Γ_{5u} type is largest at the X point and second largest at the R point. Hence, the interaction for phase IV is not relevant in pure CeB$_6$ without La substitution.

IV. DOPING DEPENDENCE

In order to clarify which energy band plays a major role in the experimental quadrupolar ordering, we artificially shift the chemical potential and investigate how the effective interactions $I_\gamma(\boldsymbol{q})$ vary. Such a "numerical experiment" is one of the advantages of theoretical calculations. We shifted the chemical potential by up to ± 1 eV in a rigid band treatment. The shift of the chemical potential changes the electron number per unit cell by -0.6 for $\Delta\mu = -1$ eV and $+0.9$ for $\Delta\mu = +1$ eV, while the $4f$ electron number is unchanged. Therefore, electron (hole) doping per boron is 0.15 (0.10) at $\Delta\mu = +1$ eV (-1 eV). The Fermi surface are changed as follows: Under the hole doping, the open Fermi surface centered at X point are closed (the dispersion on Γ–M line in Fig. 5 leaves away from E_F). On the other hand, the electron doping generates small electron pockets on Γ–M line, and hence another contribution to the susceptibility is expected.

Figure 9 shows the variation of the effective interactions $I_\gamma(\boldsymbol{q})$ as a function of $\Delta\mu$. We plotted only relevant interactions: the Γ_{5g}-quadrupole and the Γ_{2u}-octupole at R point and Γ point, and the Γ_{3g}-quadrupole and the Γ_{4u}-octupole at the M point. The leading interaction $I_Q(\boldsymbol{q}_R)$ for $\Delta\mu = 0$ is enhanced by the hole doping

($\Delta\mu < 0$). Therefore, we conclude that the Fermi surface around the X point causes the experimental quadrupolar ordering. Upon further hole doping, the octupolar interaction of Γ_{4u} type becomes dominant.

On the other hand, $I_Q(\boldsymbol{q}_R)$ is suppressed by electron doping ($\Delta\mu > 0$), which leads to a reduction of the transition temperature of phase II. Instead, the same multipole with a different $\boldsymbol{q}$-vector, namely, the Γ_{5g}-type ferroquadrupolar interaction $I_Q(\boldsymbol{0})$ is enhanced. Upon further electron doping, the quadrupolar interaction of Γ_{3g} type at the M point takes the place of the leading interaction. Our theory thus predicts that the the quadrupolar order in phase II is robust against hole doping but is replaced by other order parameters upon electron doping.

V. SUMMARY

We demonstrated a microscopic derivation of multipolar ordering using the DFT+DMFT method. There are three parameters in these calculations: U, J_H, and $\Delta\epsilon_f$. We showed a recipe to fix them: ϵ_f is determined from the PES spectrum, and $U - J_H$ can be determined from BIS spectrum. By fixing J_H to a typical value, we can thus determine these parameters in an unbiased manner.

We evaluated the $\boldsymbol{q}$-dependent multipolar susceptibilities and interactions in CeB$_6$ by solving the BS equation. Although direct observation of the second-order phase transition is practically difficult at present, we can estimate the transition temperature by extrapolating the susceptibility to low temperatures. Our results yield a good estimate.

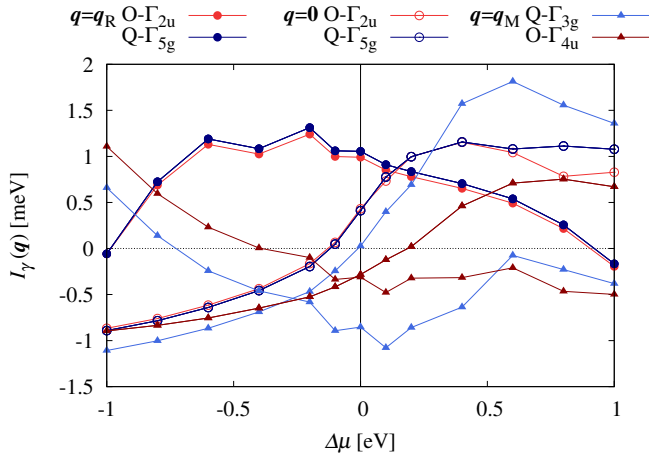Comparing our approach to the more traditional com-

FIG. 9. Variations of relevant effective interactions $I_\gamma(\boldsymbol{q})$ against the shift of the chemical potential, $\Delta\mu$. The symbols indicate the $\boldsymbol{q}$-vector: closed circles for the R point, open circles for the Γ point, and closed triangles for the M point.

FIG. 10. Calculated Δ_- and Δ_+ as a function of $\Delta\epsilon_f$ for $U = 6.0\,\text{eV}$ and $J_H = 0.8\,\text{eV}$. The horizontal dashed lines indicate the target values, $\Delta_- = 1.9\,\text{eV}$ and $\Delta_+ = 3.1\,\text{eV}$. The vertical dashed line indicates the value of $\Delta\epsilon_f$ estimated by the Hartree energy.

bination of multiorbital Kondo lattice model and RKKY formula, there are a few advantages to the new method: (i) We base our calculations on the full DFT+DMFT spectral function so that the validity of our calculation can already be checked at the single particle level by comparing to photoemission spectroscopy experiment. (ii) Our approach is free from highly compound specific parameters that need to be determined from experiment; with only two local interaction parameters U and J_H and a binding energy of the single f electron, the method can be applied to numerous Ce compounds. (iii) Our calculation procedure based on the DFT+DMFT method is not limited to highly localized f electron systems but can be also applied to itinerant f electron systems. The only difference to the calculations in this paper is the impurity solver: We have to use more sophisticated impurity solvers such as the continuous-time quantum Monte Carlo method [95] to incorporate the formation of heavy-fermion states. Interesting applications include a hidden order in URu_2Si_2 and scalar order in $PrFe_4P_{12}$ [47]. These are two of the many possible future uses of our method.

ACKNOWLEDGMENTS

Appendix A: Determination of parameters U, J_H, and $\Delta\epsilon_f$

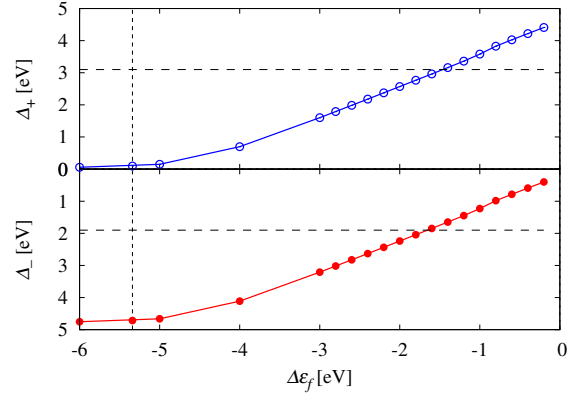We present the procedure of determining three parameters U, J_H, and $\Delta\epsilon_f$ so that Δ_- and Δ_+ agree the target

values. We first vary $\Delta\epsilon_f$ with U and J_H fixed at $6.0\,\text{eV}$ and $0.8\,\text{eV}$. Figure 10 shows Δ_- and Δ_+ as a function of $\Delta\epsilon_f$. The lower graph for Δ_- is plotted with an inverted y-axis because of the definition $\Delta_- = -E_1$. We find that the target value $\Delta_- = 1.9\,\text{eV}$ is obtained at $\Delta\epsilon_f = -1.6\,\text{eV}$. For information, when we estimate $\Delta\epsilon_f$ from the Hartree energy, we obtained $\Delta\epsilon_f \approx -5.3\,\text{eV}$, which yields unphysically deep $4f$ level.

Next, we turn our attention to Δ_+. The sum $\Delta_- + \Delta_+$ (the difference between $4f^1$ and $4f^2$ peaks in $A(\omega)$) depends on $U - J_H$, because Δ_+ is the excitation energy from E_F to the Hund' ground state of the $4f^2$ configuration. Hence, the choice of U and J_H themselves are arbitrary. Following Ref. [89], we fix $J_H = 0.8\,\text{eV}$ and vary U. Then, we found that $U = 6.2\,\text{eV}$ gives the target value $\Delta_+ = 3.1\,\text{eV}$.

Appendix B: Calculation of the effective interaction

Direct calculation of Eq. (7) is unstable because the charge fluctuation is tiny (or zero within the computer accuracy) and the inversion of the matrices $\hat{\chi}_{\text{loc}}$ and $\hat{\chi}_{\text{loc}}$ diverges. Actually, this divergence is canceled out to yield finite result. We present here how to avoid this instability.

We decompose χ_{loc} using the singular value decomposition (SVD). Since χ_{loc} is hermitian, SVD is reduced to diagonalization

$$\hat{\chi}_{\text{loc}} = USU^\dagger, \tag{B1}$$

where U is a unitary matrix, and S is a diagonal matrix whose diagonal elements (singular values) are positive and aligned in descending order. It is clear from the above expression that small singular values make the matrix inversion unstable. Suppose that the smallest singular value is zero, then we eliminate it and the corre-
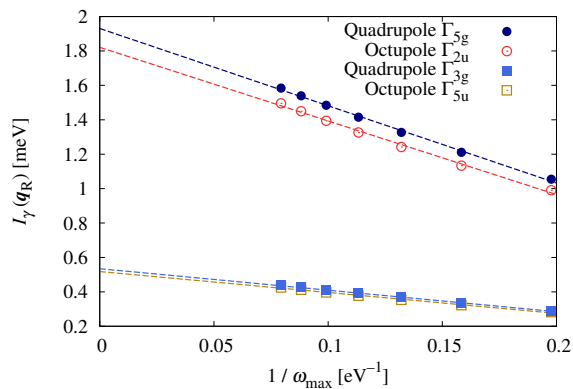
FIG. 11. Four leading effective interactions $I_\gamma(\boldsymbol{q})$ at $\boldsymbol{q} = \boldsymbol{q}_R$ as a function of $1/\omega_{max}$. The dashed lines show the result of linear fitting.

sponding basis from U. In this singular space, S and U are replaced, respectively, with an $[(M-1) \times (M-1)]$

diagonal matrix $\tilde{S}$ and $[M \times (M-1)]$ matrix $\tilde{U}$. Eq. (7) is then expressed as

$$\hat{I}(\boldsymbol{q}) \simeq \tilde{U}[\tilde{S}^{-1} - (\tilde{U}^\dagger \hat{\chi}(\boldsymbol{q})\tilde{U})^{-1}]\tilde{U}^\dagger. \qquad \text{(B2)}$$

This expression does not suffer from numerical instability.

Appendix C: Extrapolation of the frequency cutoff

We solved the BS equation for $\chi(\boldsymbol{q})$ by introducing the cutoff ω_{max} for the fermionic Matsubara frequency. In this Appendix, we present extrapolation to $\omega_{max} \to \infty$. Figure 11 shows the effective interaction $I_\gamma(\boldsymbol{q}_R)$ as a function of $1/\omega_{max}$. The data are well approximated by a line as indicated by the dashed lines. Thus, extrapolation to $1/\omega_{max} \to 0$ yields $I_\gamma(\boldsymbol{q}_R) \approx 1.93\,\text{meV}$ for the Γ_{5g}-type quadrupolar interaction.

More elaborate methods for solving the BS equation have been proposed [40, 96–99]. These approaches make the convergence faster or may allow us to obtain converged results without extrapolation.

[1] A. Georges, G. Kotliar, W. Krauth, and M. J. Rozenberg, Dynamical mean-field theory of strongly correlated fermion systems and the limit of infinite dimensions, Rev. Mod. Phys. **68**, 13 (1996).

[2] G. Kotliar, S. Y. Savrasov, K. Haule, V. S. Oudovenko, O. Parcollet, and C. A. Marianetti, Electronic structure calculations with dynamical mean-field theory, Rev. Mod. Phys. **78**, 865 (2006).

[3] M. Imada and T. Miyake, Electronic Structure Calculation by First Principles for Strongly Correlated Electron Systems, J. Phys. Soc. Jpn. **79**, 112001 (2010).

[4] K. Held, Electronic structure calculations using dynamical mean field theory, Adv. Phys. **56**, 829 (2007).

[5] E. Gorelov, M. Karolak, T. O. Wehling, F. Lechermann, A. I. Lichtenstein, and E. Pavarini, Nature of the Mott transition in Ca$_2$RuO$_4$, Phys. Rev. Lett. **104**, 226401 (2010).

[6] S. Backes, T. C. Rödel, F. Fortuna, E. Frantzeskakis, P. Le Fèvre, F. Bertran, M. Kobayashi, R. Yukawa, T. Mitsuhashi, M. Kitamura, K. Horiba, H. Kumigashira, R. Saint-Martin, A. Fouchet, B. Berini, Y. Dumont, A. J. Kim, F. Lechermann, H. O. Jeschke, M. J. Rozenberg, R. Valentí, and A. F. Santander-Syro, Hubbard band versus oxygen vacancy states in the correlated electron metal SrVO$_3$, Phys. Rev. B **94**, 241110 (2016).

[7] C. Ahn, A. Cavalleri, A. Georges, S. Ismail-Beigi, A. J. Millis, and J.-M. Triscone, Designing and controlling the properties of transition metal oxide quantum materials, Nat. Mater. **20**, 1462 (2021).

[8] M. Aichhorn, L. Pourovskii, V. Vildosola, M. Ferrero, O. Parcollet, T. Miyake, A. Georges, and S. Biermann, Dynamical mean-field theory within an augmented plane-wave framework: Assessing electronic correlations in the iron pnictide LaFeAsO, Phys. Rev. B **80**, 085101 (2009).

[9] Z. P. Yin, K. Haule, and G. Kotliar, Magnetism and charge dynamics in iron pnictides, Nat. Phys. **7**, 294 (2011).

[10] J. Ferber, H. O. Jeschke, and R. Valentí, Fermi surface topology of LaFePO and LiFeP, Phys. Rev. Lett. **109**, 236403 (2012).

[11] K. Haule, C.-H. Yee, and K. Kim, Dynamical mean-field theory within the full-potential methods: Electronic structure of CeIrIn$_5$, CeCoIn$_5$, and CeRhIn$_5$, Phys. Rev. B **81**, 195107 (2010).

[12] H. Lu and L. Huang, Pressure-driven $4f$ localized-itinerant crossover in heavy-fermion compound CeIn$_3$: A first-principles many-body perspective, Phys. Rev. B **94**, 075132 (2016).

[13] H. Ebert, D. Ködderitzsch, and J. Minár, Calculating condensed matter properties using the KKR-Green's function method—recent developments and applications, Rep. Prog. Phys. **74**, 096501 (2011).

[14] G. Rohringer, H. Hafermann, A. Toschi, A. A. Katanin, A. E. Antipov, M. I. Katsnelson, A. I. Lichtenstein, A. N. Rubtsov, and K. Held, Diagrammatic routes to nonlocal correlations beyond dynamical mean field theory, Rev. Mod. Phys. **90**, 025003 (2018).

[15] R. Sakuma, P. Werner, and F. Aryasetiawan, Electronic structure of SrVO$_3$ within GW+DMFT, Phys. Rev. B **88**, 235110 (2013).

[16] J. M. Tomczak, M. Casula, T. Miyake, and S. Biermann, Asymmetry in band widening and quasiparticle lifetimes in SrVO$_3$: Competition between screened exchange and local correlations from combined GW and dynamical mean-field theory GW + DMFT, Phys. Rev. B **90**, 165138 (2014).

[17] Z. Y. Meng, Y. B. Kim, and H.-Y. Kee, Odd-Parity Triplet Superconducting Phase in Multiorbital Materi-

als with a Strong Spin-Orbit Coupling: Application to Doped Sr_2IrO_4, Phys. Rev. Lett. **113**, 177003 (2014).

[18] A. Galler, P. Thunström, P. Gunacker, J. M. Tomczak, and K. Held, Ab initio dynamical vertex approximation, Phys. Rev. B **95**, 115107 (2017).

[19] H. Lee, K. Foyevtsova, J. Ferber, M. Aichhorn, H. O. Jeschke, and R. Valentí, Dynamical cluster approximation within an augmented plane wave framework: Spectral properties of srvo$_3$, Phys. Rev. B **85**, 165103 (2012).

[20] J. Kuneš, I. Leonov, P. Augustinský, V. Křápek, M. Kollar, and D. Vollhardt, LDA+DMFT approach to ordering phenomena and the structural stability of correlated materials, Eur. Phys. J. Special Topics **226**, 2641 (2017).

[21] A. Lichtenstein, M. Katsnelson, V. Antropov, and V. Gubanov, Local spin density functional approach to the theory of exchange interactions in ferromagnetic metals and alloys, J. Magn. Magn. Mater. **67**, 65 (1987).

[22] S. V. Halilov, H. Eschrig, A. Y. Perlov, and P. M. Oppeneer, Adiabatic spin dynamics from spin-density-functional theory: Application to Fe, Co, and Ni, Phys. Rev. B **58**, 293 (1998).

[23] A. I. Lichtenstein, M. I. Katsnelson, and G. Kotliar, Finite-Temperature Magnetism of Transition Metals: An ab initio Dynamical Mean-Field Theory, Phys. Rev. Lett. **87**, 067205 (2001).

[24] I. Leonov, A. I. Poteryaev, V. I. Anisimov, and D. Vollhardt, Electronic Correlations at the α-γ Structural Phase Transition in Paramagnetic Iron, Phys. Rev. Lett. **106**, 106405 (2011).

[25] A. S. Belozerov, I. Leonov, and V. I. Anisimov, Magnetism of iron and nickel from rotationally invariant hirsch-fye quantum monte carlo calculations, Phys. Rev. B **87**, 125138 (2013).

[26] A. Szilva, M. Costa, A. Bergman, L. Szunyogh, L. Nordström, and O. Eriksson, Interatomic exchange interactions for finite-temperature magnetism and nonequilibrium spin dynamics, Phys. Rev. Lett. **111**, 127204 (2013).

[27] T. Nomoto, T. Koretsune, and R. Arita, Local force method for the ab initio tight-binding model: Effect of spin-dependent hopping on exchange interactions, Phys. Rev. B **102**, 014444 (2020).

[28] W. E. Pickett, A. J. Freeman, and D. D. Koelling, Local-density-functional approach to the isostructual γ-α transition in cerium using the self-consistent linearized-augmented-plane-wave method, Phys. Rev. B **23**, 1266 (1981).

[29] K. Held, A. K. McMahan, and R. T. Scalettar, Cerium Volume Collapse: Results from the Merger of Dynamical Mean-Field Theory and Local Density Approximation, Phys. Rev. Lett. **87**, 276404 (2001).

[30] A. K. McMahan, K. Held, and R. T. Scalettar, Thermodynamic and spectral properties of compressed Ce calculated using a combined local-density approximation and dynamical mean-field theory, Phys. Rev. B **67**, 075108 (2003).

[31] O. Sakai, Y. Shimizu, and Y. Kaneta, Band Calculation for Ce-Compounds on the basis of Dynamical Mean Field Theory, J. Phys. Soc. Jpn. **74**, 2517 (2005).

[32] N. Lanatà, Y.-X. Yao, C.-Z. Wang, K.-M. Ho, J. Schmalian, K. Haule, and G. Kotliar, $\gamma-\alpha$ isostructural transition in cerium, Phys. Rev. Lett. **111**, 196801 (2013).

[33] E. Pavarini, E. Koch, and A. I. Lichtenstein, Mechanism for Orbital Ordering in $KCuF_3$, Phys. Rev. Lett. **101**, 266405 (2008).

[34] J. Musshoff, G. Zhang, E. Koch, and E. Pavarini, Linear-response description of superexchange-driven orbital ordering in K_2CuF_4, Phys. Rev. B **100**, 045116 (2019).

[35] M. Matsumoto, M. J. Han, J. Otsuki, and S. Y. Savrasov, First-principles simulations of heavy Fermion cerium compounds based on the Kondo lattice, Phys. Rev. Lett. **103**, 096403 (2009).

[36] K. Haule and G. Kotliar, Arrested Kondo effect and hidden order in URu_2Si_2, Nat. Phys. **5**, 796 (2009).

[37] H. Shinaoka, S. Hoshino, M. Troyer, and P. Werner, Phase diagram of pyrochlore iridates: All-in–all-out magnetic ordering and non-fermi-liquid properties, Phys. Rev. Lett. **115**, 156401 (2015).

[38] S. Mandal, K. Haule, K. M. Rabe, and D. Vanderbilt, Systematic beyond-DFT study of binary transition metal oxides, npj Comput. Mater. **5**, 115 (2019).

[39] H. Fujiwara, K. Terashima, J. Otsuki, N. Takemori, H. O. Jeschke, T. Wakita, Y. Yano, W. Hosoda, N. Kataoka, A. Teruya, M. Kakihana, M. Hedo, T. Nakama, Y. Ōnuki, K. Yaji, A. Harasawa, K. Kuroda, S. Shin, K. Horiba, H. Kumigashira, Y. Muraoka, and T. Yokoya, Anomalously large spin-dependent electron correlation in the nearly half-metallic ferromagnet CoS_2, Phys. Rev. B **106**, 085114 (2022).

[40] J. Kuneš, Efficient treatment of two-particle vertices in dynamical mean-field theory, Phys. Rev. B **83**, 085102 (2011).

[41] Z. P. Yin, K. Haule, and G. Kotliar, Spin dynamics and orbital-antiphase pairing symmetry in iron-based superconductors, Nat. Phys. **10**, 845 (2014).

[42] H. U. R. Strand, M. Zingl, N. Wentzell, O. Parcollet, and A. Georges, Magnetic response of Sr_2RuO_4: Quasi-local spin fluctuations due to Hund's coupling, Phys. Rev. B **100**, 125120 (2019).

[43] D. Geffroy, J. Kaufmann, A. Hariki, P. Gunacker, A. Hausoel, and J. Kuneš, Collective modes in excitonic magnets: Dynamical mean-field study, Phys. Rev. Lett. **122**, 127601 (2019).

[44] J. H. Shim, K. Haule, and G. Kotliar, Modeling the Localized-to-Itinerant Electronic Transition in the Heavy Fermion System $CeIrIn_5$, Science **318**, 1615 (2007).

[45] J. Otsuki, H. Kusunose, and Y. Kuramoto, Evolution of a Large Fermi Surface in the Kondo Lattice, Phys. Rev. Lett. **102**, 017202 (2009).

[46] J. Otsuki, Competing d-Wave and p-Wave Spin-Singlet Superconductivities in the Two-Dimensional Kondo Lattice, Phys. Rev. Lett. **115**, 036404 (2015).

[47] Y. Kuramoto, H. Kusunose, and A. Kiss, Multipole Orders and Fluctuations in Strongly Correlated Electron Systems, J. Phys. Soc. Jpn. **78**, 072001 (2009).

[48] E. Zirngiebl, B. Hillebrands, S. Blumenröder, G. Güntherodt, M. Loewenhaupt, J. M. Carpenter, K. Winzer, and Z. Fisk, Crystal-field excitations in CeB_6 studied by Raman and neutron spectroscopy, Phys. Rev. B **30**, 4052 (1984).

[49] T. Fujita, M. Suzuki, T. Komatsubara, S. Kunii, T. Kasuya, and T. Ohtsuka, Anomalous specific heat of CeB_6, Solid State Commun. **35**, 569 (1980).

[50] H. Nakao, K.-i. Magishi, Y. Wakabayashi, Y. Murakami, K. Koyama, K. Hirota, Y. Endoh, and S. Kunii, Antiferro-Quadrupole Ordering of CeB_6 Studied by Resonant X-Ray Scattering, J. Phys. Soc. Jpn. **70**, 1857 (2001).

[51] Y. Tanaka, U. Staub, K. Katsumata, S. W. Lovesey, J. E. Lorenzo, Y. Narumi, V. Scagnoli, S. Shimomura, Y. Tabata, Y. Onuki, Y. Kuramoto, A. Kikkawa, T. Ishikawa, and H. Kitamura, Direct and quantitative determination of the orbital ordering in CeB$_6$ by X-ray diffraction, Europhys. Lett. **68**, 671 (2004).

[52] P. Y. Portnichenko, A. Akbari, S. E. Nikitin, A. S. Cameron, A. V. Dukhnenko, V. B. Filipov, N. Y. Shitsevalova, P. Čermák, I. Radelytskyi, A. Schneidewind, J. Ollivier, A. Podlesnyak, Z. Huesges, J. Xu, A. Ivanov, Y. Sidis, S. Petit, J.-M. Mignot, P. Thalmeier, and D. S. Inosov, Field-angle-resolved magnetic excitations as a probe of hidden-order symmetry in CeB$_6$, Phys. Rev. X **10**, 021010 (2020).

[53] J. Effantin, J. Rossat-Mignod, P. Burlet, H. Bartholin, S. Kunii, and T. Kasuya, Magnetic phase diagram of CeB$_6$, J. Magn. Magn. Mater. **47-48**, 145 (1985).

[54] T. Tayama, T. Sakakibara, K. Tenya, H. Amitsuka, and S. Kunii, Magnetic Phase Diagram of Ce$_x$La$_{1-x}$B$_6$ Studied by Static Magnetization Measurement at Very Low Temperatures, J. Phys. Soc. Jpn. **66**, 2268 (1997).

[55] K. Kubo and Y. Kuramoto, Octupole Ordering Model for the Phase IV of Ce$_x$La$_{1-x}$B$_6$, J. Phys. Soc. Jpn. **73**, 216 (2004).

[56] D. Mannix, Y. Tanaka, D. Carbone, N. Bernhoeft, and S. Kunii, Order parameter segregation in ce$_{0.7}$la$_{0.3}$b$_6$: 4f octupole and 5d dipole magnetic order, Phys. Rev. Lett. **95**, 117206 (2005).

[57] H. Kusunose and Y. Kuramoto, Evidence for Octupole Order in Ce$_{0.7}$La$_{0.3}$B$_6$ from Resonant X-ray Scattering, J. Phys. Soc. Jpn. **74**, 3139 (2005).

[58] S. Nakamura, T. Goto, and S. Kunii, Magnetic phase diagrams of the dense kondo compounds CeB$_6$ and Ce$_{0.5}$La$_{0.5}$B$_6$, J. Phys. Soc. Jpn. **64**, 3941 (1995).

[59] F. J. Ohkawa, Orbital Antiferromagnetism in CeB$_6$, J. Phys. Soc. Jpn. **54**, 3909 (1985).

[60] Y. Ōnuki, T. Komatsubara, P. H. P. Reinders, and M. Springford, Fermi Surface and Cyclotron Mass of CeB$_6$, J. Phys. Soc. Jpn. **58**, 3698 (1989).

[61] R. Shiina, H. Shiba, and P. Thalmeier, Magnetic-Field Effects on Quadrupolar Ordering in a Γ_8-Quartet System CeB$_6$, J. Phys. Soc. Jpn. **66**, 1741 (1997).

[62] R. Shiina, O. Sakai, H. Shiba, and P. Thalmeier, Interplay of Field-Induced Multipoles in CeB$_6$, J. Phys. Soc. Jpn. **67**, 941 (1998).

[63] H. Shiba, O. Sakai, and R. Shiina, Nature of Ce-Ce Interaction in CeB$_6$ and Its Consequences, J. Phys. Soc. Jpn. **68**, 1988 (1999).

[64] G. Sakurai and Y. Kuramoto, Multipolar Interactions in the Anderson Lattice with Orbital Degeneracy, J. Phys. Soc. Jpn. **73**, 225 (2004).

[65] G. Sakurai and Y. Kuramoto, Wavenumber Dependence of Multipolar Interactions in the Anderson Lattice, J. Phys. Soc. Jpn. **74**, 975 (2005).

[66] T. Yamada and K. Hanzawa, Derivation of RKKY Interaction between Multipole Moments in CeB$_6$ by the Effective Wannier Model Based on the Bandstructure Calculation, J. Phys. Soc. Jpn. **88**, 084703 (2019).

[67] K. Hanzawa and T. Yamada, Origin of anisotropic RKKY interactions in CeB$_6$, J. Phys. Soc. Jpn. **88**, 124710 (2019).

[68] K. Kubo and T. Hotta, Microscopic theory of multipole ordering in NpO$_2$, Phys. Rev. B **71**, 140404 (2005).

[69] Y. Iizuka, T. Yamada, K. Hanzawa, and Y. Ōno, First-Principles Study of the RKKY Interaction and the Quadrupole Order in the Pr 1-2-20 Systems PrT_2Al$_{20}$ (T = Ti, V), J. Phys. Soc. Jpn. **91**, 074708 (2022).

[70] J. Otsuki, K. Yoshimi, H. Shinaoka, and Y. Nomura, Strong-coupling formula for momentum-dependent susceptibilities in dynamical mean-field theory, Phys. Rev. B **99**, 165134 (2019).

[71] K. Koepernik and H. Eschrig, Full-potential nonorthogonal local-orbital minimum-basis band-structure scheme, Phys. Rev. B **59**, 1743 (1999).

[72] K. Tanaka, Y. Kato, and Y. Onuki, 4f-Electron Density Distribution in Crystals of CeB$_6$ at 165 K and its Analysis Based on the Crystal Field Theory, Acta Crystallographica Section B **53**, 143 (1997).

[73] H. Eschrig and K. Koepernik, Tight-binding models for the iron-based superconductors, Phys. Rev. B **80**, 104503 (2009).

[74] K. Koepernik, O. Janson, Y. Sun, and J. van den Brink, Symmetry conserving maximally projected wannier functions (2021), arXiv:2111.09652 [cond-mat.mtrl-sci].

[75] T. Hotta, Spin and orbital structure of uranium compounds on the basis of a j-j coupling scheme, Phys. Rev. B **70**, 054405 (2004).

[76] T. Hotta and H. Harima, Effective Crystalline Electric Field Potential in a j-j Coupling Scheme, J. Phys. Soc. Jpn. **75**, 124711 (2006).

[77] V. I. Anisimov, F. Aryasetiawan, and A. I. Lichtenstein, First-principles calculations of the electronic structure and spectra of strongly correlated systems: the LDA + U method, J. Phys.: Condens. Matter **9**, 767 (1997).

[78] G. Chiaia, O. Tjernberg, L. Du'o, S. De Rossi, P. Vavassori, I. Lindau, T. Takahashi, S. Kunii, T. Komatsubara, D. Cocco, S. Lizzit, and G. Paolucci, CeB$_6$ and CeCu$_6$ single crystals probed by resonant photoemission spectroscopy: A comparison between the two electronic structures, Phys. Rev. B **55**, 9207 (1997).

[79] S. Souma, H. Kumigashira, T. Ito, T. Sato, T. Takahashi, and S. Kunii, Crystal-field splitting in CeB$_6$ observed by ultrahigh-resolution photoemission spectroscopy, J. Electron Spectros. Relat. Phenomena **114-116**, 729 (2001).

[80] J. K. Lang, Y. Baer, and P. A. Cox, Study of the 4f and valence band density of states in rare-earth metals. II. Experiment and results, J. Phys. F: Met. Phys. **11**, 121 (1981).

[81] J. F. Herbst, R. E. Watson, and J. W. Wilkins, 4f excitation energies in rare-earth metals: Relativistic calculations, Phys. Rev. B **13**, 1439 (1976).

[82] J. F. Herbst, R. E. Watson, and J. W. Wilkins, Relativistic calculations of 4f excitation energies in the rare-earth metals: Further results, Phys. Rev. B **17**, 3089 (1978).

[83] H. Shinaoka, J. Otsuki, M. Kawamura, N. Takemori, and K. Yoshimi, DCore: Integrated DMFT software for correlated electrons, SciPost Phys. **10**, 117 (2020).

[84] O. Parcollet, M. Ferrero, T. Ayral, H. Hafermann, I. Krivenko, L. Messio, and P. Seth, TRIQS: A toolbox for research on interacting quantum systems, Comput. Phys. Commun. **196**, 398 (2015).

[85] M. Aichhorn, L. Pourovskii, P. Seth, V. Vildosola, M. Zingl, O. E. Peil, X. Deng, J. Mravlje, G. J. Kraberger, C. Martins, M. Ferrero, and O. Parcollet, TRIQS/DFTTools: A TRIQS application for ab initio calculations of correlated materials, Comput. Phys. Commun. **204**, 200 (2016).

[86] A. E. Antipov, I. Krivenko, and S. Iskakov, aean-

tipov/pomerol: 1.2 (2017).

[87] S. Lebègue, A. Svane, M. I. Katsnelson, A. I. Lichtenstein, and O. Eriksson, Multiplet effects in the electronic structure of light rare-earth metals, Phys. Rev. B **74**, 045114 (2006).

[88] S. Lebègue, A. Svane, M. I. Katsnelson, A. I. Lichtenstein, and O. Eriksson, Multiplet effects in the electronic structure of heavy rare-earth metals, J. Phys.: Condens. Matter **18**, 6329 (2006).

[89] I. L. M. Locht, Y. O. Kvashnin, D. C. M. Rodrigues, M. Pereiro, A. Bergman, L. Bergqvist, A. I. Lichtenstein, M. I. Katsnelson, A. Delin, A. B. Klautau, B. Johansson, I. Di Marco, and O. Eriksson, Standard model of the rare earths analyzed from the Hubbard I approximation, Phys. Rev. B **94**, 085137 (2016).

[90] P. Delange, S. Biermann, T. Miyake, and L. Pourovskii, Crystal-field splittings in rare-earth-based hard magnets: An ab initio approach, Phys. Rev. B **96**, 155132 (2017).

[91] H. Harima, O. Sakai, T. Kasuya, and A. Yanase, New interpretation of the de Haas-van Alphen signals of LaB_6, Solid State Commun. **66**, 603 (1988).

[92] A. Koitzsch, N. Heming, M. Knupfer, B. Büchner, P. Y. Portnichenko, A. V. Dukhnenko, N. Y. Shitsevalova, V. B. Filipov, L. L. Lev, V. N. Strocov, J. Ollivier, and D. S. Inosov, Nesting-driven multipolar order in CeB_6

from photoemission tomography, Nat. Commun. **7**, 10876 (2016).

[93] M. Jarrell, Hubbard model in infinite dimensions: A quantum Monte Carlo study, Phys. Rev. Lett. **69**, 168 (1992).

[94] H. Kusunose, Description of multipole in f-electron systems, J. Phys. Soc. Jpn. **77**, 064710 (2008).

[95] E. Gull, A. J. Millis, A. I. Lichtenstein, A. N. Rubtsov, M. Troyer, and P. Werner, Continuous-time monte carlo methods for quantum impurity models, Rev. Mod. Phys. **83**, 349 (2011).

[96] A. Tagliavini, S. Hummel, N. Wentzell, S. Andergassen, A. Toschi, and G. Rohringer, Efficient Bethe-Salpeter equation treatment in dynamical mean-field theory, Phys. Rev. B **97**, 235140 (2018).

[97] H. Shinaoka, D. Geffroy, M. Wallerberger, J. Otsuki, K. Yoshimi, E. Gull, and J. Kuneš, Sparse sampling and tensor network representation of two-particle Green's functions, SciPost Phys. **8**, 012 (2020).

[98] M. Wallerberger, H. Shinaoka, and A. Kauch, Solving the Bethe-Salpeter equation with exponential convergence, Phys. Rev. Research **3**, 033168 (2021).

[99] M. Kitatani, R. Arita, T. Schäfer, and K. Held, Strongly correlated superconductivity with long-range spatial fluctuations, J. Phys. Mater. **5**, 034005 (2022).